Ionization cross section of the Cu K shell by electron impact from the K threshold to 90 keV, determined on the basis of diagram lines, satellite lines, and the radiative Auger effect

Suelen F. Barros (1)

Instituto Federal de São Paulo, Rua Primeiro de Maio 500, Bairro Estação, CEP:08571-050 Itaquaquecetuba, SP, Brazil and Universidade de São Paulo, Instituto de Física, Rua do Matão 1371, Cidade Universitária, CEP:05508-090 São Paulo, SP, Brazil

Kai L. Dardengo

Instituto Federal de São Paulo, Rua Primeiro de Maio 500, Bairro Estação, CEP:08571-050 Itaquaquecetuba, SP, Brazil

Nora L. Maidana, Alessio Mangiarotti, and Vito R. Vanin

Universidade de São Paulo, Instituto de Física, Rua do Matão 1371, Cidade Universitária, CEP:05508-090 São Paulo, SP, Brazil

José M. Fernández-Varea

Universitat de Barcelona, Facultat de Física (FQA and ICC), Diagonal 645, ES-08028 Barcelona, Catalonia, Spain and Universidade de São Paulo, Instituto de Física, Rua do Matão 1371, Cidade Universitária, CEP:05508-090 São Paulo, SP, Brazil

(Received 29 January 2025; accepted 28 May 2025; published 16 June 2025)

The Cu K ionization cross section by electron impact has been measured in the energy range from the K-shell threshold to 90 keV. To this end, a thin Cu film deposited on a thin C backing has been employed. The x rays emitted by the target have been detected by two silicon drift detectors placed at front and back angles with respect to the direction of the incident beam, which allowed us to better assess the peak fit procedure of the Kmultiplet. A careful analysis of the Cu K x-ray spectra generated by electron bombardment has been conducted, including not only the diagram lines but also the satellite lines and the counts that come from the radiative Auger effect. This enabled us to obtain the $K\alpha$ and $K\beta$ x-ray production cross sections with relative uncertainties of the order of 5%, and the K-shell ionization cross section with a precision around 7.5%. We show that, in most cases, the ionization cross sections reported according to current practice cannot be compared with the available theoretical calculations because the latter do not account for multiple-ionization effects. Our results agree with the distorted-wave Born approximation only when the K x-ray counts from satellite lines, which amount to about 20% of the total, are excluded.

DOI: 10.1103/cwp8-7zhm

I. INTRODUCTION

The accurate knowledge of ionization cross sections of atomic (sub)shells by electron impact is important for a better understanding of electron-atom interactions, which is a primary goal in basic research [1], allowing the validation of different theoretical approaches. Moreover, crosssection databases implemented in Monte Carlo simulation packages [2-7] find applications in areas such as the design of radiation detectors, the characterization of medical x-ray sources, astrophysics, and fusion plasma physics, as well as quantification by electron probe microanalysis, Auger electron spectroscopy, and electron energy-loss spectroscopy.

Although inner-shell ionization cross sections by electron impact have been the subject of research for more than a century, this topic is far from being exhausted. There is incomplete experimental and theoretical comprehension about the dependence of various inner (sub)shell ionization cross sections on the atomic number Z and on the electron incident

energy E. For instance, the Cu K ionization cross section has been measured before but with large uncertainties, typically 10%-20%, and considerable discrepancies among the data obtained by different researchers and between theory and experiment still remain [1].

The first measurement of the Cu K ionization cross section was apparently carried out by Fischer and Hoffmann in 1967 [8] with 50 keV electrons. Between 1970 and 2001 several groups performed Cu K-shell ionization experiments, mostly for 10–30 keV electrons [9–17]. Comparing these works it can be seen that the measurements of Davis *et al.* [10] and Llovet et al. [16] are systematically above (by 40% and 10%, respectively) the others. Between 40 and 100 keV there are fewer data. To the best of our knowledge, the latest experiment in this energy interval was done in 1987 [13] for 100 keV electrons, and the discrepancies between the existing experimental values are greater than at lower energies. Recently, Nazhmudinov *et al.* [18] measured the Cu *K* electron-impact ionization cross section at energies very far away from the K ionization threshold, at 1 and 2 GeV, to investigate the saturation of the cross section caused by the density effect.

^{*}Contact author: suelen.barros@ifsp.edu.br; suelenb@if.usp.br

In addition to the aforementioned problems, the methodology employed in these Cu K-shell ionization crosssection measurements is not totally clear, which makes it difficult to compare data from different researchers and with theoretical predictions. The experimental publications often do not describe unambiguously which x-ray lines were considered in the data analysis leading to the Cu K ionizations cross section. That is, they do not explain if and how satellite lines [19,20] and the counts arising from the radiative Auger effect (RAE) [21] were incorporated in the deconvolution of the peaks in the spectra, in the determination of the x-ray production cross sections, and finally in the extraction of the K-shell ionization cross section. In recent years, great effort has been devoted to quantifying these secondary effects, which are present in the x-ray spectra and directly affect the x-ray production cross sections, especially for elements with atomic numbers $19 \leqslant Z \leqslant 30$, where they might be more significant [22-29].

When an electron decays from an outer shell to fill an inner-shell vacancy in the presence of a spectator hole, the distortion of the atomic energy levels caused by the latter vacancy should be larger for the outer shells than for the inner ones. Consequently, for a given *K* diagram transition the associated satellite lines are more intense for lower atomic numbers [25]. Equivalently, for a given element, the satellite emission is anticipated to be enhanced for lines involving external shells. Thus, the characterization of these structures is particularly necessary to (1) estimate accurately the area of the peaks of the K x-ray multiplet, (2) correctly estimate and subtract the continuous component of the spectrum below the entire Kgroup, and (3) determine the $K\alpha$ and $K\beta$ x-ray production cross sections and the K-shell ionization cross section with uncertainties below 10%. However, apparently there are no in-depth studies about the experimental measurements of the Cu K ionization cross section that account for the satellite lines and the RAE.

This work is one more step in the renewed efforts to provide ionization cross-section data in the energy interval from 10 to 100 keV with a better precision than that of all available data, as well as to discuss the inconsistencies in the theoretical and experimental values found in the literature [30,31]. Specifically, the purpose of the present paper is to furnish experimental Cu $K\alpha$ and $K\beta$ x-ray production cross sections and the Cu K ionization cross section by means of a complete characterization of the Cu K x-ray multiplet, considering not only the diagram lines but also the satellite lines and the RAE in the function used to fit the x-ray energy spectrum.

Cu has been selected owing to its interest for practical purposes, and therefore greater need for an experimental arrangement and an adequate analysis methodology to guarantee uncertainties lower than the discrepancies observed between the existing measurements. To achieve this goal, aside from the improvements in the experimental arrangement described in Refs. [30,31], the present measurements have been done with two detectors simultaneously. Moreover, the total charge incident on the target during the irradiation and the areal density of Cu in the target have been double checked. This is to better evaluate the fitting function at two intensities of the important bremsstrahlung component in the spectra and

to rule out possible systematic errors that may appear in this type of measurement.

The rest of the article is structured as follows. The experimental method and subsequent data-analysis procedure are explained in Secs. II and III, respectively. Section IV presents the measured x-ray production and ionization cross sections and discusses the results. Our conclusions are summarized in Sec. V.

II. EXPERIMENT

The K-shell ionization cross section of Cu (Z=29) has been deduced from the characteristic $K\alpha$ x-ray production cross section at the (10–100) keV electron beam line of the São Paulo Microtron (São Paulo, Brazil) having recourse to a thin self-supporting Cu/C target. Details about the experimental setup can be found in Refs. [30–32].

A. Preparation and characterization of the target

The Cu/C target has been manufactured by sputtering from a metallic Cu disk onto a thin C backing. In this technique, Ar ions formed by an electric field are accelerated towards a cathode composed of the target material. The atoms detached from the Cu surface by collisions are deposited on the C substrate. A magnetic field that is perpendicular to the electric one confines the secondary electrons generated in a volume close to the cathode to increase the ionization of the gas and, therefore, the sputtering yield. The target area has been limited to a circle 8 mm in diameter by means of a mask used during the preparation. The target frame is rectangular, made of C fiber, with dimensions $30 \times 15 \times 0.5 \,\mathrm{mm}^3$, and with a circular central opening 10 mm in diameter [32].

Rutherford backscattering spectrometry (RBS) has been employed to estimate the areal density (number of atoms per unit surface) of the Cu film and the C backing. These measurements have been conducted at the LAMFI/IFUSP Pelletron tandem accelerator [33]. The target, placed at the center of the irradiation chamber and tilted 7° relative to the direction of the incident beam, has been irradiated with a 2200(11) keV ⁴He⁺ beam, around 1.8 mm in diameter, hitting its center.

The areal densities of the Cu and C films have been deduced from the energy spectra of the elastically backscattered ⁴He ions recorded with a surface barrier Si detector positioned at 120° relative to the ion beam direction by means of the MultiSIMNRA program [33], which is based on SIMNRA calculations [34]. Figure 1 shows the energy spectra of the backscattered ⁴He ions and the corresponding simulated MultiSIMNRA spectrum for the Cu/C target. Besides the Cu film and C backing the target contains O and S. Cu undergoes oxidation in contact with atmospheric air. Although the target has been stored in a chamber filled with N₂ gas, during its handling it came into contact with atmospheric air, and part of it appears to be oxidized to copper sulphate. The amount of O and S in the sample has been estimated from the RBS spectra and is $(\mathcal{N}d)_0 = 4.9(7) \times 10^{16}$ atoms/cm² and $(\mathcal{N}d)_S =$ $1.3(3) \times 10^{16}$ atoms/cm², respectively. These values confirm that the oxidation of the target was not complete but possibly affected only its outermost surface.

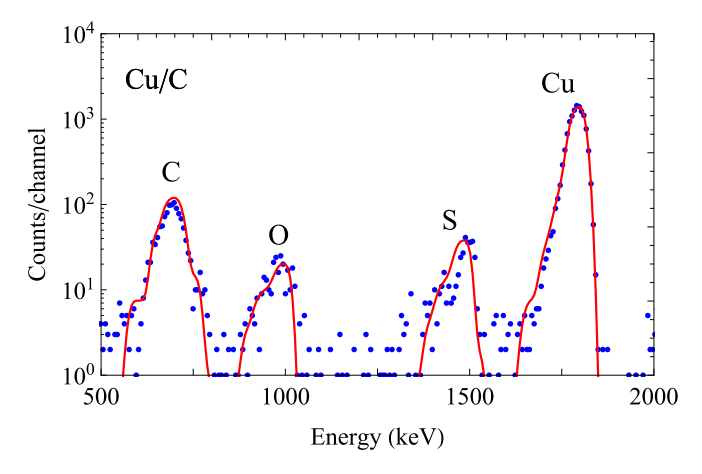


FIG. 1. Experimental (blue dots) and simulated (red curve) energy spectra of the ⁴He ions backscattered elastically from the Cu/C target, irradiated with a 2200(11) keV ⁴He⁺ beam. The spectrometer gain is around 6.5 keV/channel.

As discussed in Ref. [30], the uncertainties of the areal density of Cu estimated with the procedure described above come from three sources: (1) the spectrum acquisition, (2) the MultiSIMNRA spectrum simulation, and (3) the nonuniformity of the target. For the Cu/C target the relative standard deviations of the first two sources of uncertainties are 5.8% and 1.5%, respectively. In turn, to estimate the uniformity of the Cu film, measurements have been performed with the $2200(11)\,\mathrm{keV}^4\mathrm{He}^+$ beam hitting the target at several points slightly away from its center, namely, about 2 mm below, to the left, above, and to the right of it. The results are displayed in Fig. 2. The standard deviation of these areal densities yields an estimate of the nonuniformity of $4.7\times10^{15}\,\mathrm{Cu}$ atoms/cm² for the sample.

The outcome of this characterization is an areal density of Cu equal to $(\mathcal{N}d)_{\text{Cu}} = 1.58(7) \times 10^{17} \text{ atoms/cm}^2$, which would correspond to a 16.7(7) µg/cm² mass thickness of pure Cu. On the other hand, the mass thickness of the C backing is $10.2(9) \text{ µg/cm}^2$.

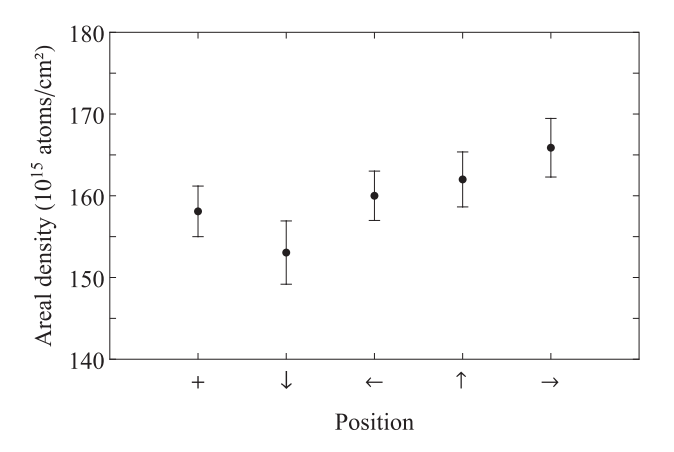


FIG. 2. Areal densities of the Cu film in five positions of the Cu/C target obtained by RBS. The abscissa identifies the irradiation point: + is the target center whereas \downarrow , \leftarrow , \uparrow , and \rightarrow denote points 2 mm below, to the left, above, and to the right of the target center, respectively.

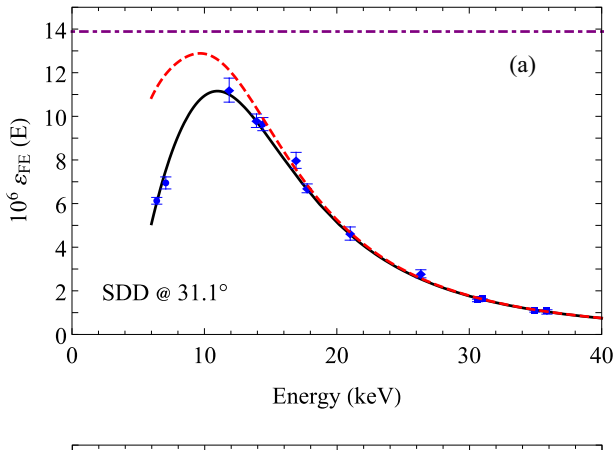
B. X-ray detection

The x-ray production measurements have been carried out inside a cylindrical irradiation chamber 490 mm in diameter and 220 mm in height, whose lateral wall is made of stainless steel whereas the lower and upper lids are made of aluminum. At 0° relative to the incident electron beam direction there is a Faraday cup made of graphite, shaped as a truncated cone with a half-aperture angle of 12.0(5)° and 200 mm deep [32]. The Faraday cup and the irradiation chamber are electrically insulated, and two current integrators connected to them collect the incident electrons. This arrangement allowed the determination of the total charge incident on the target during each irradiation and also the fraction of electrons scattered by the target that reach the Faraday cup (see below).

The x rays emitted from the target in each run have been detected simultaneously by two silicon drift detectors (SDDs; Amptek, Bedford, MA, USA) used in pile-up rejection mode. These SDDs have a 0.5-mm-thick Si crystal with a 25 mm² front face covered by an internal collimator with an open area of 17 mm² (nominal values). The 12.7- μ m-thick Be window is separated by 1.4 mm from the front surface of the active volume. The detectors have been placed outside the irradiation chamber at 31.1(5)° and 125.0(5)° with respect to the beam direction, 12.5(5) mm away from the spectroscopy windows and 312(2) mm from the target. The energy resolutions [full width at half maximum (FWHM)] were 133 eV and 136 eV at the energy of the Fe $K\alpha$ x rays (6.4 keV) for the SDDs placed at the front and back angles, respectively.

The SDDs have been calibrated in energy and full-energy (FE) peak efficiency resorting to certified point radioactive sources of 57 Co ($\gamma_{14\,\mathrm{keV}}$; Fe $K\alpha$ and $K\beta$ x rays), 133 Ba (Cs $K\alpha$ and $K\beta$ x rays), and 241 Am ($\gamma_{26\,\mathrm{keV}}$; Np $L\ell$, $L\alpha$, and $L\beta$ x rays). The intensities of the lines were taken from Ref. [35], except for the Np L x rays, for which the values given in Ref. [36] and, exclusively for the $L\ell$ line, in Ref. [37], have been employed.

The FE peak efficiencies, ε_{FE} , of the spectrometers have been determined by means of an analytical model developed by Seltzer [38,39], whose adjustable parameters are the fraction of solid angle subtended by the detector, $\Omega/(4\pi \text{ sr})$, and the thickness \mathcal{L} of the Si crystal. These parameters have been fitted to the experimental FE peak efficiency values deduced from the net areas of γ -ray and x-ray peaks in the spectra acquired with the radioactive sources placed in the center of the irradiation chamber, i.e., at the same position occupied by the Cu/C target when it is irradiated by the electron beam [38,39]. During the calibration measurements with the radioactive sources the chamber is filled with air, unlike the target irradiation conditions, when the chamber is evacuated to a pressure of 7×10^{-5} Pa. The fitted values in this experiment are $\hat{\Omega}/(4\pi \text{ sr}) = 1.39(17) \times 10^{-5}$ and $\hat{\mathcal{L}} = 0.4983(7) \text{ mm}$ for the detector at 31.1(5)°, and the parameters for the detector at $125.0(5)^{\circ}$ are $\hat{\Omega}/(4\pi \text{ sr}) = 1.39(15) \times 10^{-5}$ and $\hat{\mathcal{L}} =$ 0.4957(5) mm. The estimated crystal thicknesses \mathcal{L} are in excellent agreement with the nominal value of 0.5 mm quoted by the manufacturer [40]. Figure 3 depicts the experimental FE peak efficiency values along with the $\varepsilon_{FE}(E)$ curves calculated with the fitted parameters in the analytical model and the attenuating layers appropriate to the two experimental



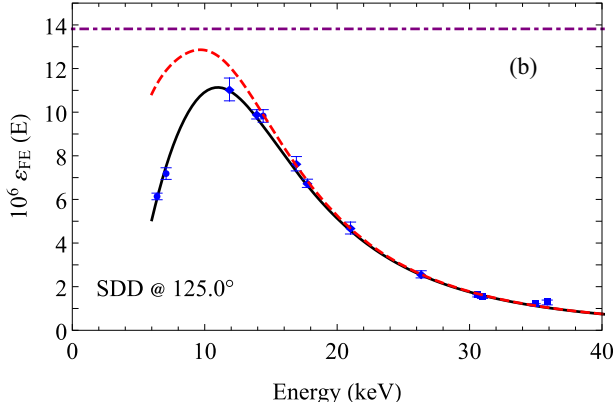


FIG. 3. FE peak efficiencies, $\varepsilon_{\rm FE}(E)$, of the SDDs as a function of photon energy for the detector placed at (a) $31.1(5)^{\circ}$ and (b) $125.0(5)^{\circ}$. The symbols are experimental values (circles are points from the $^{57}{\rm Co}$ source, diamonds from the $^{241}{\rm Am}$ source, and squares from the $^{133}{\rm Ba}$ source); the uncertainty bars correspond to one standard deviation. The continuous and dashed curves are Seltzer's model [38,39] computed with the fitted values, $\hat{\mathcal{L}}$ and $\hat{\Omega}$ (see the text), in the experimental conditions of the measurement with the radioactive sources (chamber filled with air) and with the electron beam (vacuum in chamber), respectively. The (purple) horizontal dot-dashed lines indicate the geometrical efficiencies $\hat{\Omega}/(4\pi~{\rm sr})$.

configurations, namely, during the measurements with radioactive sources (the chamber is filled with air at atmospheric pressure) and during the irradiations (the chamber is evacuated).

C. X-ray spectra measurements

Electrons with energy in the interval 9–90 keV have been supplied by the electron gun of the São Paulo Microtron (Instituto de Física, Universidade de São Paulo, Brazil). The electrical current of the beam has been selected between 2 μ A and 6 μ A in accordance with the x-ray counting rate, which ranged from 3 kcps to 8 kcps, so that the dead time was lower than 6% in all irradiations. The counting times have been maintained between 600 s and 1200 s, yielding $K\alpha$ peaks with $\sim 10^7 - 10^8$ counts. Figure 4 shows the spectra recorded by the two SDDs for the run with 11.53(9) keV electrons. Note the higher bremsstrahlung contribution at forward angles.

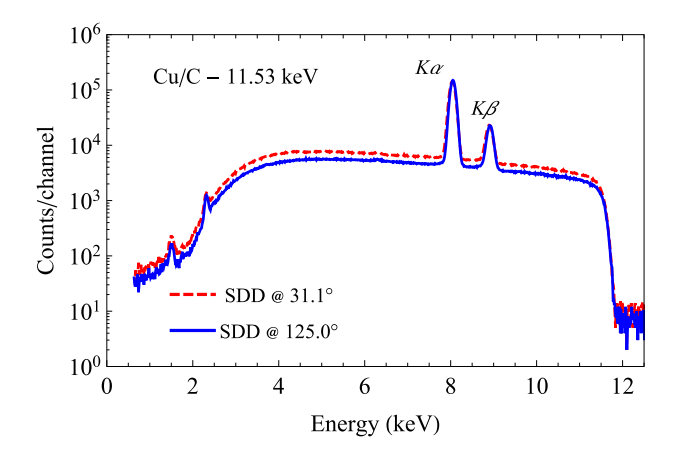


FIG. 4. X-ray spectra measured with the SDDs placed at $31.1(5)^{\circ}$ (red dashed curve) and $125.0(5)^{\circ}$ (blue solid curve) relative to the incident beam direction, for electrons with 11.53(9) keV. The spectrometer gains are 13.04 eV/channel and 12.76 eV/channel for the detectors at $31.1(5)^{\circ}$ and $125.0(5)^{\circ}$, respectively.

The total charge impinging on the target has been established, with an accuracy better than 0.5%, summing the charges collected in the Faraday cup and in the irradiation chamber [32]. The dead times have been estimated following Ref. [41], with relative uncertainties around 2% for the mentioned counting rates.

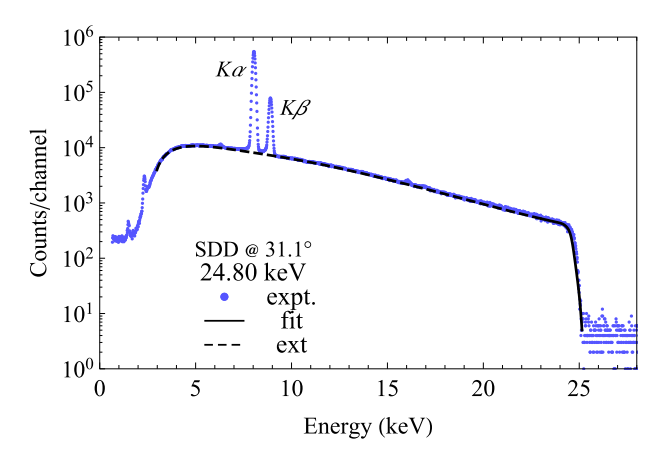
III. DATA ANALYSIS

A. Electron-beam energies

In the 9–50 keV interval the energies of the electron beam and their uncertainties have been estimated from the fit of the parameters of an analytical model to the bremsstrahlung spectrum tip [42]. This model is built from the convolution of the detector's response function with the theoretical bremsstrahlung spectrum emitted by the target [43,44]. The adjustable parameters of the model are the average and the width of the Gaussian electron-beam energy distribution and the bremsstrahlung yield, and they have been fitted to the experimental bremsstrahlung spectrum in the tip region. For energies above 50 keV, the value delivered by the voltmeter connected to the electron gun has been chosen because the FE peak efficiency of the SDDs decreases rapidly (see Fig. 3). Figure 5 displays the experimental x-ray spectra corresponding to the irradiation with 24.80(9) keV electrons together with the extrapolation of the curves calculated with the parameters fitted to the tip of the bremsstrahlung spectra from the tip down to the energies of the K x rays.

B. X-ray peak areas

The K x-ray spectra have been fitted using an approach similar to that described in Refs. [31,45] for the L lines of high-Z atoms. The parameters of the entire K group have been fitted simultaneously to the net spectrum deduced by subtracting from the measured one the contributions of pile-up [38], Si K x-ray escape [39], and an approximate bremsstrahlung component underneath the K multiplet [42]. The latter has been calculated with the parameters fitted in the procedure



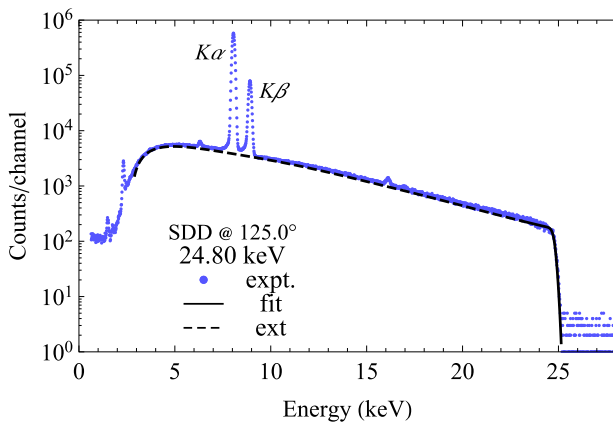


FIG. 5. X-ray energy spectra emitted by the Cu/C target bombarded with 24.80(9) keV electrons. The (blue) dots denote the experimental spectra, the continuous curves are the values calculated with the theoretical model and the fitted parameters, and the dashed ones correspond to the theoretical prediction extrapolated outside the fit region. The pile-up of $K\alpha$ x rays produced the small peaks slightly above 16 keV. The spectrometer gains are 13.04 eV/channel and 12.76 eV/channel for the detectors at $31.1(5)^{\circ}$ and $125.0(5)^{\circ}$, respectively.

employed to estimate the electron-beam energy (below 50 keV) or with the experimental areal density of the Cu film and the energy measured with the voltmeter (above 50 keV).

In our earlier investigations on K-shell and L-subshell ionization cross sections we only included diagram lines in the function that fitted the relevant multiplet to be analyzed [30,31,45]. However, for transition elements with $19 \le Z \le 30$ that have partially filled 3d and 3s subshells, some phenomena generate counts that appear in the spectra close to the diagram lines: the presence of an extra vacancy during the radiative transition [19,25], the RAE [21], and exchange interactions that can occur between the 3p and 3d electrons [23,46,47]. All of them perturb the shape of the K multiplet and cannot be neglected, especially in spectra recorded with good-resolution detectors and high counting statistics, as in the present experiment [22,25].

The fit function implemented for the discrete component of the Cu *K* x-ray spectra has been constructed contemplating three physical phenomena:

(i) Main x-ray lines or diagram lines: due to x rays that are emitted by atoms when one inner-shell vacancy is filled by a radiative transition [23,28,29]. The lines that have been included in our fit function are $K\alpha_1$ ($1s_{1/2} \rightarrow 2p_{3/2}$), $K\alpha_2$ ($1s_{1/2} \rightarrow 2p_{1/2}$), $K\beta_1$ ($1s_{1/2} \rightarrow 3p_{3/2}$), $K\beta_3$ ($1s_{1/2} \rightarrow 3p_{1/2}$), and $K\beta_5^{\rm I.II}$ ($1s_{1/2} \rightarrow 3d_{3/2}$, $3d_{5/2}$); the last is a forbidden transition in the dipole approximation, but it is visible in the recorded spectra.

(ii) Radiative Auger effect (RAE): corresponding to counts that come from an electron transition with the simultaneous emission of a photon and an Auger electron [21]. The x ray shares its energy with the ejected electron, hence its energy is lower than that of the corresponding diagram line. The RAE competes with the emission of the diagram lines and gives rise to separate lines, called radiative Auger satellites (RASs), which are placed on the low-energy side of the main peak. The RASs follow the same denomination as the usual Auger effect, namely, three letters (plus subindices, if needed) that indicate the sequence of (sub)shells pertaining to the initial vacancy, the relaxing electron, and the ejected Auger electron, e.g., KLL, KLM, and KMM [21,22].

(iii) Satellite lines: corresponding to x rays that are generated in the presence of a spectator hole when an electron decays from an outer shell to fill an inner-shell vacancy. The extra hole causes a change in electron configuration and modifies the energy of the emitted photon. Also, since the natural width depends on the lifetime of the state through the uncertainty principle, initial hole states in the presence of multiple vacancies have a significant increase in the natural width compared to the diagram lines because they tend to have a shorter lifetime.

Spectator vacancies can be created by four mechanisms: shake up, shake off, TS1, and TS2. The first two are one-step mechanisms that correspond to the promotion of an atomic electron to an outer shell (shake up) or to the continuum (shake off) owing to the sudden change in the atomic potential caused by the rapid removal of an inner-shell electron. On the other hand, TS1 and TS2 are two-step mechanisms; in TS1 the ejected electron interacts with another bound electron from the same atom creating a new vacancy, while in TS2 the two vacancies are generated consecutively by the same incident particle. The probability of occurrence of one-step mechanisms should be independent, in first order, of the incident particle, while the two-step ones depend on the energy and type of projectile [24,25]. The satellite lines that explain the asymmetry of the Cu K lines are assumed to be caused mainly by shake-off processes [26,27].

Several researchers have investigated during the last twenty years the energy, intensity, and natural width of the K satellite transitions induced by the impact of photons [48,49], protons [50], and electrons [23,25,28,29]. They have also looked into the physical phenomena that originate each of them. Here we rely on the results of Refs. [28,29] for the satellite lines included in the $K\alpha$ and $K\beta$ groups.

It is important to emphasize that the RAE is responsible for around 2% of the counts in the entire Cu K multiplet, while the satellite lines are around 20% of the $K\alpha$ and $K\beta$ peaks. These percentages can be even larger for other elements with Z in the range $19 \leqslant Z \leqslant 30$ [22,24–27].

In the $K\alpha$ group two 3d satellite contributions have been included: $K\alpha_{12}$ that comes from the $1s_{1/2} \rightarrow 2p_{3/2}$ transition in the presence of a spectator hole in the 3d subshell, $K\alpha_{22}$ resulting from the transition $1s_{1/2} \rightarrow 3p_{1/2}$ with a spectator hole also in the 3d subshell, and one 2p satellite, $K\alpha''$ (or $K\alpha_{3,4}$), despite its low intensity [23,28,51].

Conversely, the situation for the $K\beta$ x-ray multiplet is not yet fully understood. One of the best characterizations of this multiplet, using single- and double-crystal spectrometers, resorted to a sum of five Lorentzians to describe it [23,52]. The agreement between the fit function and the measured spectrum was good, but the physical meaning of each Lorentzian was not specified. A similar picture emerged in other studies on satellite lines in the $K\beta$ group of elements with $12 \le Z \le 30$ [25,27,29].

The energy resolutions of our SDDs are not adequate to separate all these nondiagram lines, but their good FE peak efficiency allowed us to record spectra with a high statistics, around 10^7 – 10^8 counts in the $K\alpha$ peak. Then to achieve a satisfactory fit it is crucial that the second-order effects are not neglected in the model function proposed for the investigated peaks. We have followed Ref. [29], including six peaks for the $K\beta$ group. Three of them are the diagram lines $K\beta_1$, $K\beta_3$, and $K\beta_5^{1,II}$ whereas the other three come from radiative transitions in the presence of spectator vacancies, denoted as $K\beta_c$, $K\beta_d$, and $K\beta_e$.

The peaks belonging to diagram or satellite lines have been described by a Voigt function, i.e., the convolution of the response function of the spectrometer (a Gaussian) with the natural shape of an x-ray line (a Lorentzian), see Ref. [39] and Refs. cited therein. The Gaussian dispersion associated with the detector FWHM is given by $\sqrt{s_{\rm el}^2 + W_{\rm Si} F_{\rm Si} E}$ [38], where $s_{\rm el}$ is the standard deviation of the electronic noise introduced by the pulse amplification, whereas W_{Si} and F_{Si} are the average energy expended in the formation of an electron-hole pair in Si and the Fano factor [53], respectively. The product W_{Si} F_{Si} has been set equal to the value fitted to the peaks in the energy and efficiency calibration with the radioactive sources, and $s_{\rm el}$ has been treated as a free parameter for each run. In turn, for the natural width of the Lorentzian profile we resorted to the values from Refs. [28,29] and the spectrometer's gain. Furthermore, a smoothed step towards lower energies has been added for each diagram line.

The RAS distribution has been described employing a function that corresponds to the convolution of an exponential with a Gaussian [54–56]:

$$I_i^{\text{RAS}} = \frac{1}{2} I_i \lambda e^{\lambda (E - E_0 + \lambda \sigma^2 / 2)}$$

$$\times \operatorname{erfc} \left(\frac{E - E_0 + \lambda \sigma^2}{\sqrt{2}\sigma} \right), \quad i = \alpha, \beta, \quad (1)$$

where λ is the decay factor, I_i is the amplitude factor associated with the number of RAE counts in the $K\alpha$ and $K\beta$ peaks, respectively, E_0 is the edge energy, σ is the dispersion associated with the detector's response function, and erfc is the complementary error function. The residual continuous component of the spectra has been described by a second-degree polynomial.

The parameters of the model function in the $K\alpha$ and $K\beta$ groups have been fitted simultaneously, which is crucial to get estimates that describe the continuous component of the spectrum realistically. To this end, the K multiplet has been split into two blocks. In the first one, the $K\alpha_1$ position has been left free, whereas the positions of the $K\alpha_2$ diagram line and the $K\alpha_{12}$, $K\alpha_{22}$, and $K\alpha_{3,4}$ satellite lines have been fixed relative to it. In the second one, the position regarded as a free parameter was that of the $K\beta_1$ line, and those of the $K\beta_3$, $K\beta_5^{I,II}$, $K\beta_c$, $K\beta_d$, and $K\beta_e$ lines have been tied to it. The relative positions have been determined from the spectrometer's gain and the experimental radiative transition energies measured by Melia and co-workers [28,29], except for the $K\beta_5^{I,II}$ line, for which the value has been extracted from Ref. [57], and are listed in Table I. In both blocks, the counts resulting from the RAE have been modeled with Eq. (1).

The number of counts of the peak with the highest intensity in each block, namely, $K\alpha_1$ in the first one and $K\beta_1$ in the second one, and the parameters of the total number of counts due to the RAE in the $K\alpha$ and $K\beta$ peaks, $I_{K\alpha}$ and $I_{K\beta}$, respectively, have been regarded as free parameters in the fit whereas the others have been fixed in relation to the relative intensities $A_{K\alpha_i}/A_{K\alpha_1}$ (i = 12, 22, 34) and $A_{K\beta_i}/A_{K\beta_1}$ (j = 1, 3, 5, c, d, e) for the blocks that contain the $K\alpha_1$ and $K\beta_1$ lines, respectively. To this end, the relative intensities of Melia et al. [28,29] have been adopted, except for the $K\beta_5^{\rm I,II}$ line for which the value has been taken from Ref. [58]. Note that fixing the relative intensities of the satellite lines assumes that most of them arise from one-step mechanisms and do not depend on the incident particle or on the beam energy [25–27]. Indeed, previous research suggests that the dominant mechanisms in the emission of satellite lines are the shake or TS1 processes [24]. The contribution of TS2 events to the total counts in the K group of Cu is expected to be less than 1% [60]. For instance, Mauron and Dousse [60] measured the cross section of TS2 processes as a function of the electron beam energy for three elements. In the case of Co, whose atomic number (Z = 27) is close to that of Cu, σ_{TS2} increases up to \approx 13 keV and then stays approximately constant.

The RAE is disregarded in the fit function proposed by Melia *et al.* [28] to describe the Cu $K\alpha$ multiplet. However, according to Ref. [22] the contribution of the RAE is around 1% of the $K\alpha$ peak area. Therefore, we have decided to model this x-ray group by adding a contribution for the RAS [Eq. (1)] to the functions that describe the diagram and satellite lines.

Two strategies have been employed to evaluate the fit quality. First, the reduced chi square of the fit, together with the normalized residual, has been evaluated when the RASs have been included in both blocks, $K\alpha$ and $K\beta$, and when it has been taken into account only in the $K\beta$ group, for both detectors; see Fig. 6. Second, since the reduced chi square was smaller when the RAS model was included in both blocks, we decided to examine the energy dependence of the ratios $\Gamma_{K\beta}/\Gamma_{K\alpha}$ and I_i/Ki ($i=\alpha,\beta$) [see Eq. (1)] which come from these fits. These ratios are depicted in Fig. 7 along with the values found in the literature. The net experimental energy spectra corresponding to the irradiation with a 28.41(7) keV electron beam are plotted in Fig. 8 alongside the curves calculated with the fitted parameters.

TABLE I. Energies, relative intensities, and natural width for Cu obtained from Refs. [28,29]. For the $K\beta_5$ the values have been extracted from Deslattes *et al.* [57] for energy, Scofield [58] for intensity, and Krause and Oliver [59] for natural width. The numbers in parentheses are the uncertainties (one standard deviation) in units of the last significant digits.

Line	Transition	<i>E</i> (eV)	Γ (eV)	I (%)
$K\alpha_1$	$1s_{1/2} \to 2p_{3/2}$	8047.837(5)	2.261(28)	58.14(28)
$K\alpha_2$	$1s_{1/2} \to 2p_{1/2}$	8027.993(8)	2.71(3)	22.92(18)
$K\alpha_{12}$	$1s_{1/2}(3d) \to 2p_{3/2}(3d)$	8045.433(5)	2.80(3)	7.72(13)
$K\alpha_{22}$	$1s_{1/2}(3d) \to 2p_{1/2}(3d)$	8026.566(8)	3.30(4)	10.67(18)
$K\alpha_{3,4}$	$1s_{1/2}(2p) \to (2p)(2p)$	8077.5(4)	9.869	0.549(19)
$K\beta_1$	$1s_{1/2} \to 3p_{3/2}$	8905.519(11)	3.42(7)	46.9(17)
$K\beta_3$	$1s_{1/2} \to 3p_{1/2}$	8903.101(26)	3.46(7)	24.7(11)
$K\beta_5^{\mathrm{I,II}}$	$1s_{1/2} \rightarrow 3d_{3/2,5/2}$	8977.7(6)	1.55(6)	0.0065(3)
$K\beta_c$	_	8908.43(5)	3.82(26)	12.8(16)
$K\beta_d$	_	8897.66(9)	8.34(14)	10.62(29)
$K\beta_e$	_	8910.48(20)	5.42(23)	4.9(7)

The charge fraction incident on the Faraday cup has also been measured in each irradiation. This has allowed us to cross-check the charge measurements and the areal density of Cu in the Cu/C target through Monte Carlo simulations that are based on theoretical elastic scattering cross sections (see below).

C. Charge fraction incident on the Faraday cup

The electrical charge incident on the target during the irradiation has been determined by the sum of the charges recorded in the chamber and in the Faraday cup. The latter has a well-defined angular aperture, $12.0(5)^{\circ}$, hence one can estimate the charge fraction that crossed the target and hit the Faraday cup. This charge fraction has also been measured in each run.

The measurement of the charge fraction incident on the target has been carried out according to the technique described in Ref. [63], which discusses a much more complete

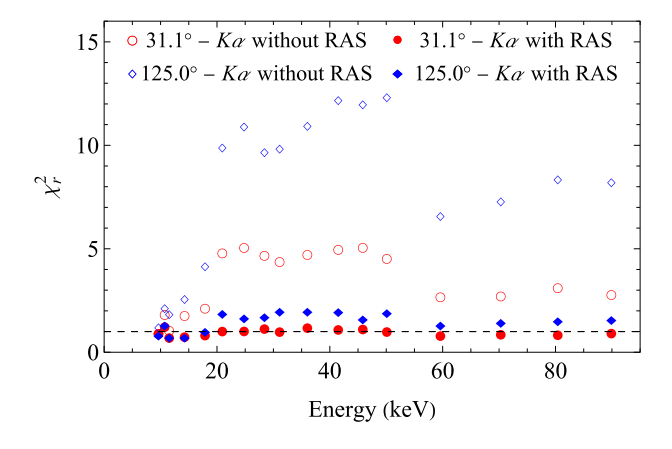


FIG. 6. Reduced chi square of the fits, χ_r^2 , from the spectra acquired at $31.1(5)^\circ$ (red circles) and $125.0(5)^\circ$ (blue diamonds) as a function of the beam energy. The filled symbols correspond to the values obtained when the model function for the spectrum includes the RAS lines in the $K\alpha$ and $K\beta$ groups, and the open symbols when the fit is done with the model function excluding the RAS lines in the $K\alpha$ group.

experiment for multiple-scattering measurements. Although the experimental arrangement in the cited reference is different from the one employed here, the Faraday cup has been the same in both experiments so that it has been possible to follow the same analysis method.

Since the target consists of a thin Cu film on a thin C substrate, elastic scattering of the electrons by the Cu atoms is anticipated to be the dominant interaction mechanism. Thus, knowing the composition and thicknesses of the Cu and C films and the cross sections for elastic scattering, it is possible to run Monte Carlo simulations to estimate the fraction of electrons scattered by the target that hit the Faraday cup. The comparison of these simulations with the measured charge fractions furnishes an additional validation of the charge collection procedure during the irradiations and of the estimated thickness of the Cu film, which is proportional to its areal density, both fundamental in the determination of the x-ray production cross sections.

The simulations have been conducted employing a new version of the in-house Monte Carlo code that was developed to estimate the attenuation of the anisotropy parameter in *L* multiplets caused by the opening of the electron beam inside the target [64]. The program is written in *Mathematica* and implements elastic differential and integrated cross sections from Ref. [65].

The Monte Carlo code simulates electron trajectories in a target composed of an arbitrary number of juxtaposed thin layers of homogeneous materials limited by parallel planes. Only elastic collisions are simulated, hence the kinetic energy of the electron is constant while it traverses the target. The thickness of each layer and the elastic scattering cross section for its material are input quantities, and so are the position and direction of the electron beam impinging on the target with respect to the normal to the target plane. The core routine gives the electron path inside a single layer. Starting with the position and direction of the incident electron, it samples randomly the distance between successive elastic collisions and the direction after a collision from the integrated and differential elastic cross sections, respectively. The output of the program is a list of positions and directions of the electron trajectory inside a single layer from the entrance to the exit point, which can be any of the layer surfaces. The main routine

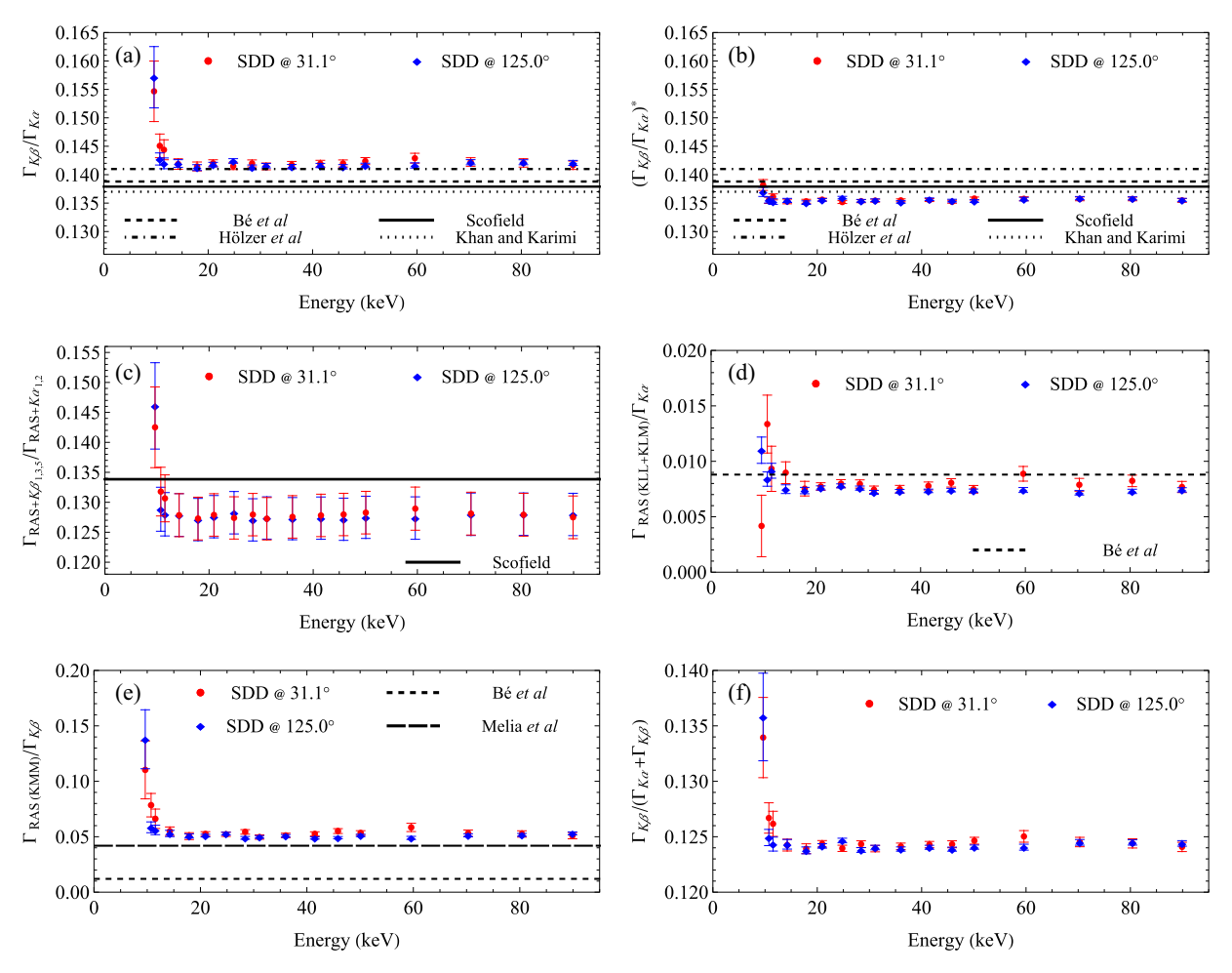


FIG. 7. Experimental ratios (a) $\Gamma_{K\beta}/\Gamma_{K\alpha}$ (including diagram lines, satellite lines, and RAE counts), (b) $(\Gamma_{K\beta}/\Gamma_{K\alpha})^*$ (including only diagram and satellite lines), (c) $(\Gamma_{K\beta_{1,3,5}} + \text{RAS})/(\Gamma_{K\alpha_{1,2}} + \text{RAS})$, (d) $I_{\alpha}/\Gamma_{K\alpha}$, (e) $I_{\beta}/\Gamma_{K\beta}$, and (f) $\Gamma_{K\beta}/\Gamma_{(K\alpha+K\beta)}$. The symbols represent the data obtained with the SDDs placed at 31.1(5)° (red circles) and 125.0(5)° (blue diamonds) relative to the electron beam direction. The horizontal lines indicate the ratios tabulated by Scofield [58] (solid lines), Bé *et al.* [22] (short-dashed lines), Melia *et al.* [29] (long-dashed lines), Hölzer *et al.* [61] (dot-dashed lines), and Khan and Karimi [62] (dotted lines).

builds a list with the electron path in the various layers of the target, tagged by the layer identification, beginning with the path inside the layer hit by the electron beam, with its characteristic direction and central position. If the electron backscatters in the first layer, the track is terminated; if it exits the opposed face, the position and direction of the exiting electron are used to build the path along the next layer. The process is iterated until one of the external layers of the target is hit by the electron. Although the program records redundant information (for instance, directions could be deduced from positions), this facilitates the analysis and reduces the code development time. Figure 9 shows the charge fractions measured in the present experiment, the values predicted by Monte Carlo simulations, and the data of Ref. [63] where the same Cu/C target was used.

D. X-ray production cross sections

The x-ray production cross section σ_{Kj}^{x} for the peak Kj in the run with electrons of energy E that impinge perpendicularly on a thin film and cross it without energy loss can be

evaluated from

$$\sigma_{Kj}^{x}(E) = \frac{N_{Kj}}{N_{e} \mathcal{N} d_{\text{eff}} \, \varepsilon_{\text{FE}}(E_{Kj})(1 - \phi)},\tag{2}$$

where N_{Kj} is the area of the Kj peak (energy E_{Kj}), N_e is the number of electrons incident on the target, \mathcal{N} is the number of Cu atoms per unit volume, d_{eff} is the effective thickness of the Cu film (see below), and ϕ is the dead time fraction during the acquisition, which has been evaluated according to Refs. [41,66].

The electrons that hit the target undergo elastic and inelastic collisions that change their energy and direction of propagation. In particular, the effective path length $d_{\rm eff}$ of the electron beam within the Cu film will be somewhat longer than its thickness d. To correct for this energy-dependent path-length increase, Monte Carlo simulations have been performed using the code described in Sec. III C. The Cu/C target was modeled including in the Cu film also the O and S atoms determined by RBS. Figure 10 presents the simulated correction factor $d_{\rm eff}(E)/d$ for our Cu film as a function of the beam energy.

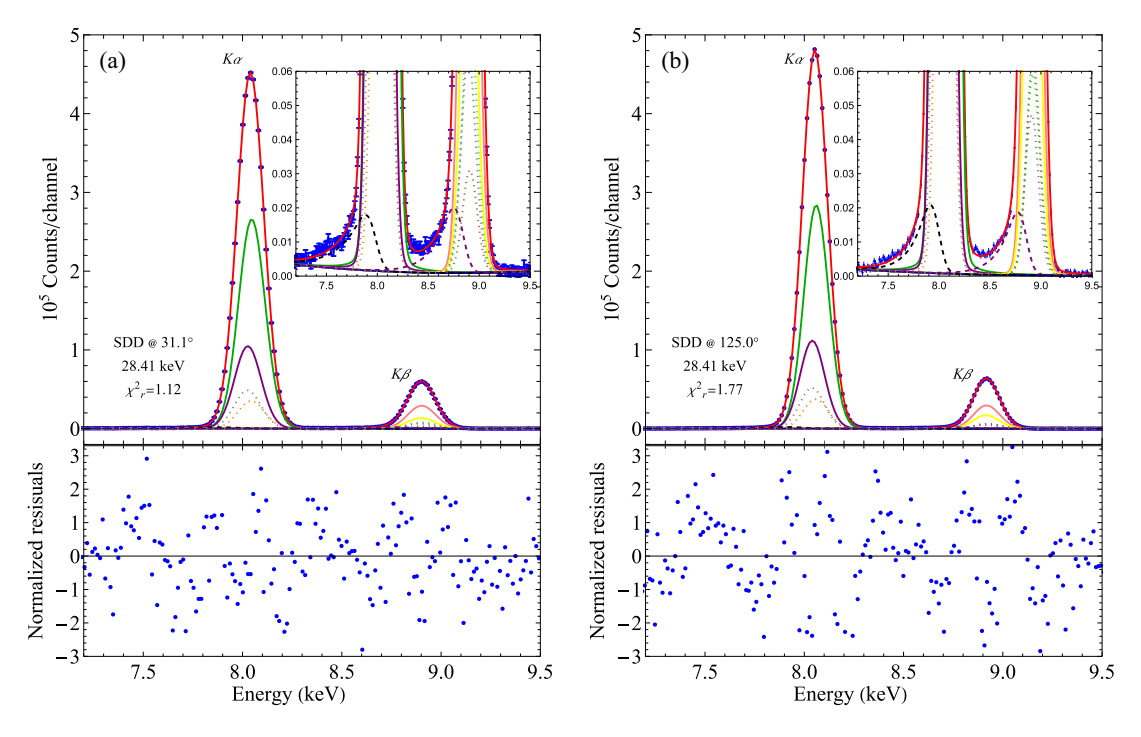


FIG. 8. Experimental spectra (dots) after removal of pile-up, Si K escape, and the evaluated bremsstrahlung distributions, with 28.41(7) keV electrons at the detection angles (a) $31.1(5)^{\circ}$ and (b) $125.0(5)^{\circ}$. The model function (solid, dotted, and dashed curves) calculated with the fitted parameters for the Cu K multiplet are also plotted. The respective χ_r^2 of the fits were 1.12 and 1.77. The dotted and dashed curves indicate the satellite lines and the RAE counts, respectively.

Although the number of energy-loss interactions (bremsstrahlung or ionization) in the target is small, electrons of 10 keV undergo an average number of five elastic collisions within the Cu layer of the target of this experiment. The elastic interactions open the electron beam and, therefore, determine its path length inside the target. Our target model includes three layers, made of copper sulfate, pure Cu, and C. The beam penetrates the target through the copper sulfate layer and exits through the C layer. This model considers the results of the RBS experiment, which indicated the presence of S and O in addition to Cu and C; see Sec. II A.

The average energy lost by the electrons in the Cu film can be inferred from its thickness and the stopping power of Cu for electrons evaluated at the incident kinetic energy. For instance, $\Delta E = 0.113$ keV for the beam with the lowest energy, 9.63(9) keV, i.e., $\Delta E/E = 0.0117$. Therefore $\Delta E/E \lesssim 1\%$. Consequently, the $K\alpha$ and $K\beta$ x-ray production cross sections have been calculated from Eq. (2) with the values of $N_{\rm e}$, $\mathcal{N}d_{\rm eff}$, and $\varepsilon_{\rm FE}(E_{Lj})$ estimated as described above.

It is important to remember that to estimate our $K\alpha$ x-ray production cross section, $\sigma_{K\alpha}^{x}$, the $K\alpha_{1}$, $K\alpha_{12}$, $K\alpha_{2}$, $K\alpha_{22}$, and $K\alpha_{3,4}$ lines, together with the RAE counts, have been employed, and for the $K\beta$ x-ray production cross sections,

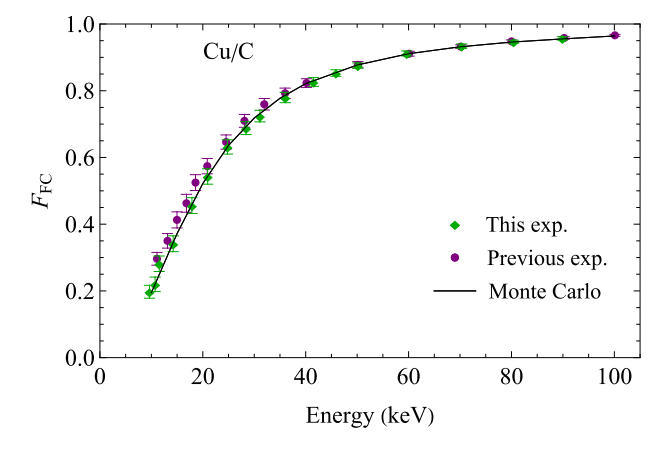


FIG. 9. Fraction of charge impinging on the Faraday cup as a function of the beam energy. The (green) diamonds are the present data and the (violet) circles are from Ref. [63]. The solid curve is the result of Monte Carlo simulations.

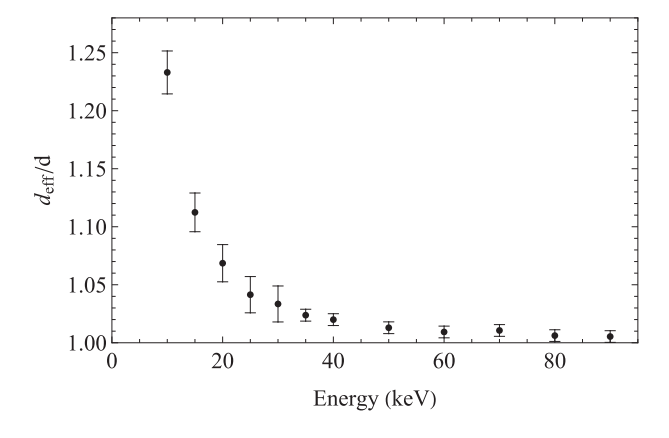


FIG. 10. Multiplicative correction factor to determine the effective path length $d_{\rm eff}$ in Cu of the electrons that impinge perpendicularly on the Cu/C target as a function of the incident beam energy.

 $\sigma_{K\beta}^{x}$, the lines taken into account along with the RAE counts have been $K\beta_{1,3}$, $K\beta_{5}$, $K\beta_{c}$, $K\beta_{d}$, and $K\beta_{e}$. That is, our x-ray production cross sections have been determined with x rays that are emitted after K-shell ionizations in which one or more vacancies have been generated, thus encompassing all estimated counts in the $K\alpha$ or $K\beta$ peaks, which corresponds to the quantity of interest in most practical applications of x-ray production cross sections. The uncertainties of $\sigma_{K\alpha}^{x}$ and $\sigma_{K\beta}^{x}$ have been found by the usual propagation method applied to Eq. (2).

E. K-shell ionization cross sections

The *K*-shell ionization cross sections have been determined by means of the relation

$$\sigma_K(E) = \sigma_{Kj}^{\chi} \left(\omega_K \frac{\Gamma_{Kj}}{\Gamma_{K\alpha} + \Gamma_{K\beta}} \right)^{-1}, \quad j = \alpha, \beta, \quad (3)$$

where ω_K is the *K*-shell fluorescence yield whereas $\Gamma_{K\alpha}$ and $\Gamma_{K\beta}$ are the $K\alpha$ and $K\beta$ x-ray emission rates, respectively.

The fluorescence yield ω_K is the probability that the filling of a K-shell vacancy be followed by a photon emission. On the other hand, the Auger yield a_K is the probability that the filling of a K-shell vacancy be followed by the ejection of an outer-shell electron [22,59]. Several compilations and evaluations of ω_K exist [67–69], but in these publications it is not disclosed how the RAE was dealt with [22,69]. Krause [69], for example, states that $\omega + a + f = 1$, where ω , a, and f are the fluorescence, Auger, and Coster-Kronig yields, respectively. Vacancies in the K shell cannot be filled by Coster-Kronig transitions, and therefore $\omega_K + a_K = 1$. Hence, we cannot ascertain whether the contribution of RAE is included in their tabulated ω_K values. Nevertheless, we have selected $\omega_K = 0.440$ as recommended by Krause [69], which is in excellent agreement with the value $\omega_K = 0.438(16)$ measured by Yashoda et al. [70] employing a ⁵⁷Co radioactive

A similar challenge is faced when choosing the emission rates to be inserted in Eq. (3). Most researchers that measured the Cu K ionization cross section took the emission rates from Refs. [58,62]. But in these Refs. it is unclear whether $\Gamma_{K\beta}/\Gamma_{K\alpha}$ was calculated including changes in the atomic potential in the presence of multiple vacancies, which give rise to satellite lines. In addition, RAE is not mentioned in these articles and it is not possible to know if this effect was contemplated in the calculated ratios of emission rates. Scofield's emission rates [58] include the multiple vacancies that are generated in the process of emission of the x ray, but not those that are produced during the ionization of the target atom, shifting the atomic energy levels and the resulting x-ray energies. For these reasons, we have picked Scofield's ratio $\Gamma_{K\beta}/\Gamma_{K\alpha} = 0.1379$ [58]; see Fig. 7(a).

IV. RESULTS AND DISCUSSION

Inspection of the normalized residuals of the fits (Fig. 8) and of the χ_r^2 (Fig. 6) demonstrates the high quality achieved in determining the peak parameters. The peak fitting methodology yields reliable estimates of both the peak counts and their uncertainties, while it also indicates that incorporating

TABLE II. $\Gamma_{K\beta}/\Gamma_{K\alpha}$, $\Gamma_{RAS(KLL+KLM)}/\Gamma_{K\alpha}$, and $\Gamma_{RAS(KMM)}/\Gamma_{K\beta}$ for Cu determined from the diagram lines, satellites lines, and RAE counts in the $K\alpha$ and $K\beta$ multiplets. The numbers in parentheses are the uncertainties (one standard deviation) in units of the last significant digits.

$\Gamma_{K\beta}/\Gamma_{K\alpha}$	$\Gamma_{\text{RAS(KLL+KLM)}}/\Gamma_{K\alpha}$	$\Gamma_{ m RAS(KMM)}/\Gamma_{K\beta}$
0.14186(18)	0.00761(11)	0.0517(6)

the RAS structure into the $K\alpha$ and $K\beta$ multiplets leads to a significant improvement. As already said, our analysis procedure assumes that the multiple vacancies in the Cu K x-ray spectra are mostly produced by one-step mechanisms, which is reasonable for a low-energy electron beam.

The comparison of the values measured in this experiment for the charge fractions incident on the Faraday cup with the simulated values employing only elastic scattering cross sections (Fig. 9) confirms that the target is thin and elastic scattering is the dominant interaction mechanism [63]. It also corroborates the areal density of Cu in the Cu/C target measured by RBS within uncertainties.

Figure 7(a) displays our results for $\Gamma_{K\beta}/\Gamma_{K\alpha}$ as a function of the beam energy. The value for this ratio estimated by the average over all energies and at both angles is given in Table II. The comparison of the present values with those calculated or measured by other authors must be done with care because each of them could have dealt with the counts in the $K\alpha$ and $K\beta$ peaks in different ways. Moreover, for elements with $19 \le Z \le 30$ this ratio may depend on the chemical and oxidation state and also on the ionization mechanism [22].

To enable a broad evaluation with the values from the previous works, we have estimated not only $\Gamma_{K\beta}/\Gamma_{K\alpha}$, which takes into account events that came from single and multiple ionizations together with the ones from RAE, but also $(\Gamma_{K\beta}/\Gamma_{K\alpha})^*$, which includes diagram lines and the lines ensuing from multiple ionization, and $(\Gamma_{K\beta_{1,3,5}+RAS})/(\Gamma_{K\alpha_{1,2}+RAS})$, which contain diagram lines and the RAE counts.

Our $\Gamma_{K\beta}/\Gamma_{K\alpha}$ ratios are approximately 3% above the value calculated by Scofield [58] [Fig. 7(a)], but his tabulated emission rates do not incorporate multiple vacancies that are generated in the ionization process. In Fig. 7(c) it can be seen that our $(\Gamma_{K\beta_{1,3,5}+RAS})/(\Gamma_{K\alpha_{1,2}+RAS})$ results, with uncertainties around 4%, are \approx 5% lower than Scofield's value [58], therefore the values reported here are in reasonable accord with those calculated by him within the error bars. The reason for the high uncertainties in the latter ratios comes from the way our fitting procedure has been done, fixing the relative intensities of the peaks with the smaller number of counts. Thus, when extracting only the area of some lines from each group, the variances of these relative fractions must be treated together with the covariance between them, but Melia *et al.* [28,29] did not furnish these covariances.

Shima *et al.* [12] did not specify the lines that were included in the $K\alpha$ and $K\beta$ peaks. Moreover, they did not quote the measured value of $\Gamma_{K\beta}/\Gamma_{K\alpha}$ but pointed out that it was within 5% of that calculated by Scofield [58].

Khan and Karimi [62] presented a set of most probable $\Gamma_{K\beta}/\Gamma_{K\alpha}$ ratios estimated on the basis of all available

experimental data. Our measurement of this ratio is about 3% above their value for Cu. But when we consider only diagram and satellite lines, excluding the RAE counts, $(\Gamma_{K\beta}/\Gamma_{K\alpha})^*$ in Fig. 7(b), our result is around 1% below Khan and Karimi's ratio.

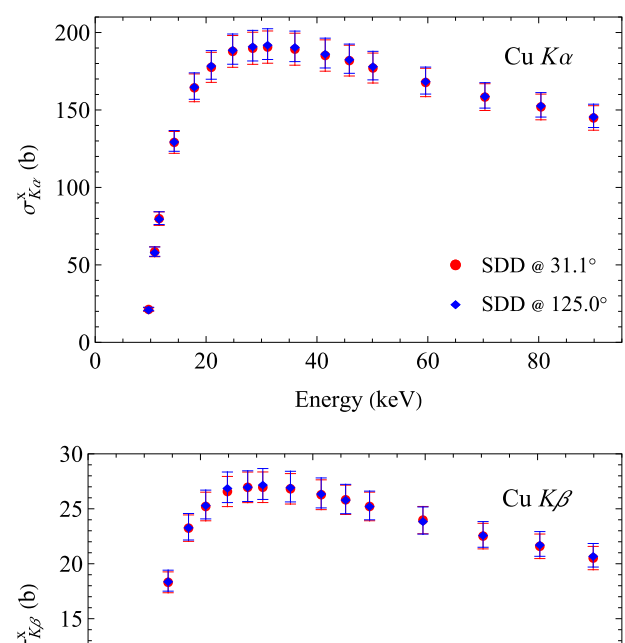
Bé *et al.* [22] used bremsstrahlung photons to produce the K vacancies, stated $K\alpha$ as containing $K\alpha_1$, $K\alpha_2$, RAE KLL, RAE KLM, $K\alpha^H$, $K\alpha'$, and $K\beta$ as containing $K\beta_{1,3}$, $K\beta_5$, $K\beta'_b$, and RAE KMM. Hence, they included in the $K\alpha$ and $K\beta$ peaks counts that come from single and multiple vacancies, in addition to those due to the RAE. In Fig. 7(a) it is possible to note that our intensity ratios calculated in this manner are around 2% above the value measured by them.

Finally, Hölzer *et al.* [61] did measurements with electrons but used a single-crystal diffractometer optimized for minimal instrumental broadening. In this reference the counts in $K\alpha$ incorporate lines $K\alpha_1$, $K\alpha_2$, $K\alpha_{12}$, and $K\alpha_{22}$, while the counts in $K\beta$ contain the $K\beta_1$ and $K\beta_3$ lines as well as the $K\beta_c$, $K\beta_d$, and $K\beta_e$ lines. RAS lines are not mentioned, but the way the peak fitting was made suggests that the RAE counts are probably being included in the areas of diagram and multiple-ionization lines. Figure 7(a) shows that our $\Gamma_{K\beta}/\Gamma_{K\alpha}$ are about 0.6% below the value measured by them.

Our result for the RASs in the $K\alpha$ peak, $\Gamma_{RAS(KLL+KLM)}/\Gamma_{K\alpha}$, listed in Table II and depicted in Fig. 7(d), is consistent with the data of Bé et al. [22]. On the other hand, for the RAS in the $K\beta$ group, $\Gamma_{RAS(KMM)}/\Gamma_{K\beta}$, our values are systematically higher than those of Bé et al. [22], aligning more closely with the ones from Melia et al. [29]; see Fig. 7(e). Bé et al. [22] described the RAS lines in the spectrum with Gaussians. Since these lines are asymmetric and have a greater contribution to the $K\beta$ group than to the $K\alpha$ group, it is anticipated that the value found by them is underestimated in the $K\beta$ multiplet, which may justify the observed discrepancy.

Figure 7 shows that close to the ionization threshold there is a slight dependence of the various ratios of emission rates on the ionization energy; however, above \approx 12 keV this dependence disappears and the values stay constant up to 90 keV. As described above, the RAS spectrum is created by a change in electronic configuration when an electron in an outer shell decays. In this process, the energy of the transition is shared by the emitted x ray and the ejected electron, but the influence of these lines to the photon spectrum is not affected by the energy of the incident particles. The RAS contribution should therefore be independent of the beam energy [71]. Figures 7(d) and 7(e) demonstrate that the fraction of RAS lines in the $K\alpha$ and $K\beta$ groups remained constant for all energies above 12 keV, which supports that the fit function employed to describe the peaks could correctly discriminate them from the other lines in the Cu K multiplet for the energy range of present concern. For energies below 12 keV, spectra with higher count statistics and measured with better resolution detectors are necessary to reduce the uncertainties and then evaluate the energy dependence of these fractions.

Concerning the anisotropy in the emission of K x-rays, it is worth noting that in the $K\alpha$ group the counts coming from multiple vacancies correspond to less than 20% of the total, while in the $K\beta$ multiplet this number is around 30%. Then, if there is any anisotropy in these groups introduced by counts



② SDD @ 31.1° SDD @ 125.0° O SDD @ 125.0° Energy (keV)

FIG. 11. Cu $K\alpha$ and $K\beta$ x-ray production cross sections as a function of electron energy. The (red) circles and (blue) diamonds are the present experimental values for the detectors at 31.1° and 125.0°, respectively. The error bars correspond to one standard deviation.

coming from multiple vacancies, as suggested in Ref. [72], it should be more prominent in the $K\beta$ multiplet.

The results of this work for the Cu $K\alpha$ and Cu $K\beta$ x-ray production cross sections are displayed in Fig. 11, and they are consistent with an isotropic x-ray emission within the 5% error bars. Thus, our estimates for $\sigma_{K\alpha}^x$ and $\sigma_{K\beta}^x$ correspond to the average value of the measurements performed at the two angles and these data are presented in Table III. Unfortunately, none of the studies that measured the Cu K ionization cross section provided $\sigma_{K\alpha}^x$ and/or $\sigma_{K\beta}^x$, which would have permitted a direct comparison of the data without the influence of emission rates and fluorescence yields.

The x-ray production cross sections determined from the measurements done at the two angles are totally consistent with each other; see Fig. 11. This is expected because the analysis procedure was conducted correctly: K x-ray emission is isotropic for K diagram lines [64], and the anisotropy introduced by lines originating from multiple vacancies ought to be small [72], lower than our 5% error bars. This result supports that the continuous component of the spectra and the FE peak efficiency curves of both detectors have been accurately quantified despite the significant difference in the bremsstrahlung spectrum recorded in the front and back positions of the detectors; see Fig. 5.

The K-shell ionization cross section has been determined from the $K\alpha$ x-ray production cross section. Table III collects

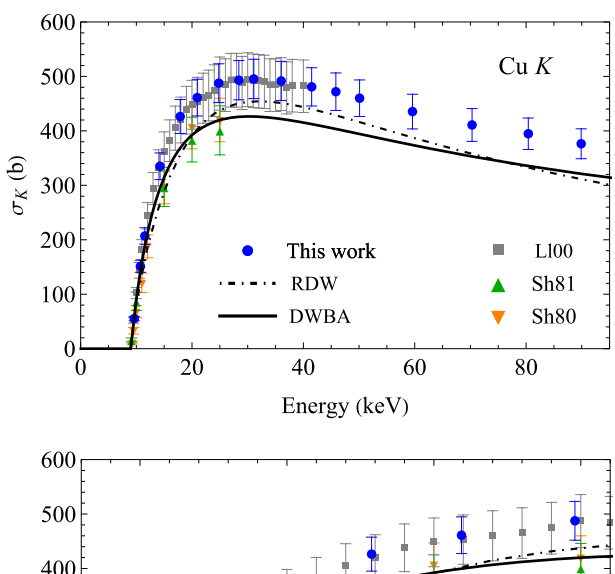
TABLE III. Electron-impact Cu $K\alpha$ and Cu $K\beta$ x-ray production cross sections and Cu K ionization cross section (in barn) as a function of beam energy (in keV), derived from diagram lines, satellites lines, and RAE counts in the $K\alpha$ and $K\beta$ groups, σ_K , and from only diagram and RAS lines (single-vacancy processes), σ_K^* . The numbers in parentheses are the uncertainties (one standard deviation) in units of the last significant digits.

E (keV)	$\sigma_{K\alpha}^{x}$ (b)	$\sigma_{K\beta}^{x}$ (b)	σ_K (b)	σ_K^* (b)
9.63(9)	21.4(12)	3.33(21)	55(4)	44(3)
10.73(9)	58.5(31)	8.4(4)	151(12)	123(9)
11.53(9)	80.0(41)	11.4(6)	207(16)	168(13)
14.25(10)	130(7)	18.4(9)	335(25)	271(21)
17.88(10)	164(9)	23.3(13)	426(32)	345(26)
20.94(11)	178(9)	25.3(14)	461(34)	372(28)
24.80(9)	188(11)	26.8(15)	487(36)	394(30)
28.41(7)	191(11)	27.0(15)	493(36)	399(30)
31.10(8)	192(11)	27.2(15)	495(37)	400(30)
36.02(4)	190(11)	26.9(15)	491(36)	397(30)
41.49(4)	186(11)	26.4(15)	480(35)	389(29)
45.84(4)	182(9)	25.8(14)	472(35)	382(29)
50.1(5)	178(9)	25.2(14)	460(34)	372(28)
59.6(5)	168(9)	24.0(13)	435(32)	352(27)
70.3(5)	158(9)	22.6(13)	411(30)	332(25)
80.4(5)	152(8)	21.7(12)	395(29)	319(24)
89.9(5)	146(8)	20.6(12)	376(28)	304(23)

our values of σ_K , which are depicted in Fig. 12 together with the older measurements and with the theoretical predictions of Bote and Salvat's distorted-wave Born approximation (DWBA) [73] and the relativistic distorted wave (RDW) approximation of Palmeri et al. [74]. These formalisms are based on the first Born approximation but differ in the treatment of the transverse interaction, the way exchange is implemented, and the wave function of the active electron. We have decided to reproduce in Fig. 12 only the Cu K ionization cross section data from the experiments that used thin targets on thin substrates and that quoted the employed fluorescence yield and emission rates, and these parameters were identical or very close to those we adopted. Our Cu K ionization cross section, σ_K , agrees with the theoretical predictions of the DWBA and the RDW only close to the ionization threshold. Above around 12 keV both of them underestimate our values by about 15%.

All magnitudes that affect the x-ray production cross section have been double checked. The FE peak efficiency model has been applied to the two detectors used in the measurements, the target thickness and the charge incident on it have been validated with the Monte Carlo simulations using elastic scattering cross sections, and the number of counts in the $K\alpha$ and $K\beta$ peaks allowed us to determine the ratio $\Gamma_{K\beta}/\Gamma_{K\alpha}$, which was consistent with the data from several papers.

However, this discussion should be made with caution because the DWBA and the RDW approximation (see Fig. 12) contemplate only single vacancies, disregarding the occurrence of multiple vacancies during the ionization. Thus, our results, as presented so far, cannot be compared with the predictions of these formalisms because the x-ray production cross sections chosen to estimate our K-shell ionization



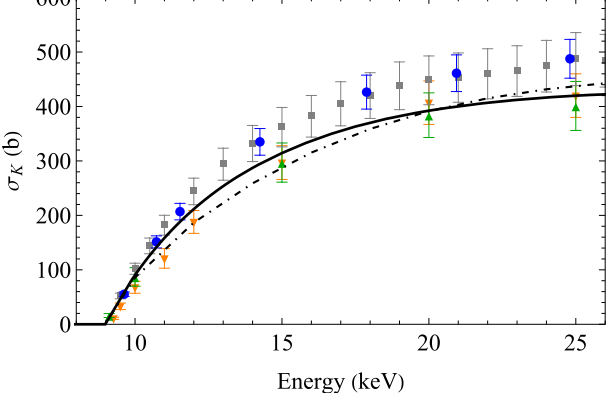


FIG. 12. Cu *K* ionization cross section (determined from the counts of diagram lines, satellite lines, and RAE) as a function of electron energy. The (blue) circles with error bars (one standard deviation) are the present experimental values. The solid and dot-dashed curves are the predictions of the DWBA [73] and the RDW approximation [74], respectively. Down and up triangles indicate the experimental data from Refs. [11] and [12], respectively, and the squares are the values from Ref. [16].

cross section include the counts in the $K\alpha_{12}$, $K\alpha_{22}$, and $K\alpha_{3,4}$ peaks, which are originated in the presence of spectator holes. Furthermore, the $\Gamma_{K\beta}/\Gamma_{K\alpha}$ ratio selected to deduce σ_K from $\sigma_{K\alpha}^{\rm x}$ also ignores the possibility of multiple vacancies during the ionization process [58] and should not be employed to estimate the K-shell ionization cross section from our $K\alpha$ x-ray production cross section.

With the aim of furnishing a meaningful comparison, including the same effects in both the theoretical predictions and the experimental results, a second set of data has been prepared for the $K\alpha$ x-ray production cross section that includes only the counts that originate from single vacancies generated in the ionization event, namely diagram lines and the RAE counts. This x-ray production cross section without multiple-vacancy counts has been employed to determine new K-shell ionization cross sections, denoted as σ_K^* . These values are shown in Fig. 13 together with the DWBA and RDW curves and the same data as in Fig. 12. Figure 13 highlights that by considering only the counts that come from single vacancies our experimental results agree within the uncertainty bars with the predictions of both formalisms.

Table IV summarizes the electron-impact Cu K ionization cross section experiments, published to date, addressing the

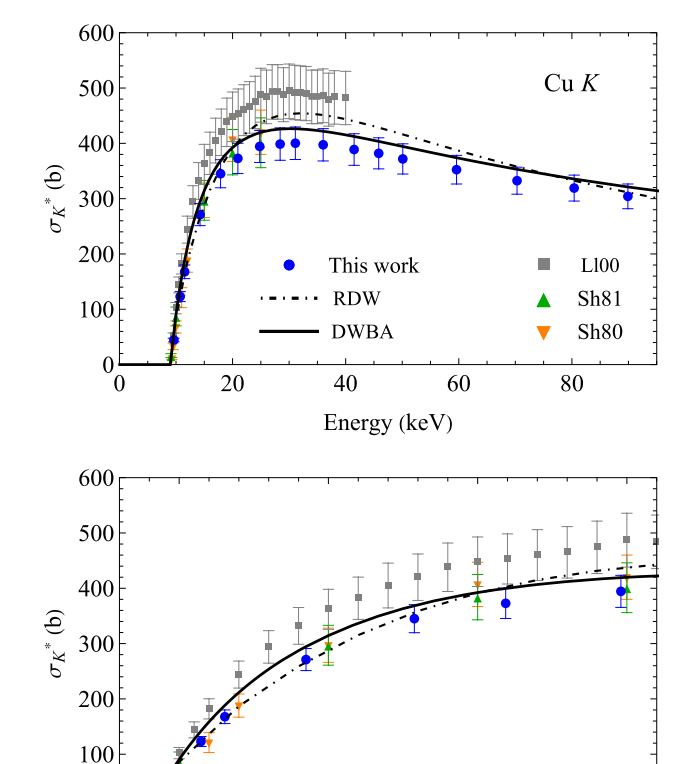


FIG. 13. Cu K ionization cross section σ_K^* , (determined from the counts of diagram and RAS lines) as a function of electron energy. The present experimental values are plotted as (blue) circles with error bars (one standard deviation). The solid and dot-dashed curves were calculated with the DWBA [73] and the RDW approximation [74], respectively. The down and up triangles indicate the experimental data from Refs. [11,12], respectively, and the squares are the values from Ref. [16].

15

Energy (keV)

10

same energy range as this work. Many authors did neither indicate which lines are included in the measurement of data analysis method of these x-ray production cross sections nor provide the values of the atomic relaxation parameters used for the final estimate of the ionization cross section, which prevents a rigorous comparison with our σ_K and σ_K^* values.

Since we have employed the same values for ω_K and $\Gamma_{K\beta}/\Gamma_{K\alpha}$ as Shima *et al.* [12] (see Table IV), our *K*-shell ionization cross section can be compared directly with that of Ref. [12]. Note in Fig. 12 that there is good agreement between our σ_K and the values by Shima [11] and Shima *et al.* [12] from the *K* threshold up to \approx 15 keV, but at higher energies our data are \approx 14% above theirs.

It is foreseen that in the vicinity of the ionization threshold the probability to produce multiple vacancies will be lower because the beam energy is low. Although it was emphasized in Ref. [12] that the Cu K ionization cross section was determined from the $K\alpha$ x rays, the authors did not say if the $K\alpha$ counts included the satellite lines or the RAE. Therefore, it is not possible to affirm that the discrepancies larger than the error bars for energies close to the ionization threshold are in fact due to multiple vacancies which are being accounted for in our $K\alpha$ counts and may not be in those of Shima *et al.* [11,12]. On the other hand, Fig. 13 reveals that when counts from multiple vacancies are disregarded in estimating the Cu K ionization cross section, our results are fully consistent with those of Shima et al. [11,12] for the entire energy range of the measurements, which suggests that these counts were excluded by the authors.

Unlike in previous studies, Westbrook and Quarles [13] estimated the Cu *K* ionization cross section from the theoretical bremsstrahlung cross section. The authors assumed that the number of counts in the characteristic x-ray peaks and in a selected bremsstrahlung energy interval present the same dependence on the target thickness, on the number of incident electrons, and on the solid angle subtended by the detector, thus the ratio between the characteristic x-ray

TABLE IV. Summary of all measurements done so far on the Cu K electron-impact ionization cross section for energies from the K threshold to ~ 100 keV, enumerated in chronological order.

25

20

Group	Detector	E (keV)	Target	ω_K	$\Gamma_{K\beta}/\Gamma_{K\alpha}$
Davis et al. [10] (1972)	Ge(Li)	20–140	Thin Cu film on a C substrate	0.545	
Shima et al. [11] (1980)	Si(Li)	9.27–25	Thin Cu film $(2.7-10 \mu\text{g/cm}^2)$ on a thin C substrate $(3 \mu\text{g/cm}^2)$	0.440	_
Shima et al. [12] (1981)	Si(Li), FWHM = 180 eV at Mn $K\alpha$ x rays	9.12–25	Thin Cu film on a thin C substrate $(7\mu\text{g}/\text{cm}^2)$	0.440	0.138
Westbrook and Quarles [13] (1987)	Si(Li) and HPGe	100	Thin Cu film $(15-60 \mu\text{g/cm}^2)$ on a thin C substrate $(15 \mu\text{g/cm}^2)$	-	-
An et al. [14] (1996)	Si(Li), FWHM = 180 eV at Mn $K\alpha$ x rays	8-25	Thin Cu film (7.6 μg/cm ²) on a thick Al substrate	0.138	0.138
He et al. [15] (1997)	Si(Li)	9–29	Cu film (15 mg/cm ²) on a thick Mylar substrate (1.37 mg/cm ²)	-	_
Llovet et al. [16] (2000)	WDS and Si(Li)	9.5–40	Thin Cu film $(1.25 \mu\text{g/cm}^2)$ on a thin C substrate $(6.8 \mu\text{g/cm}^2)$	0.441	0.137
Zhou et al. [17] (2001)	Si(Li)	10–34	Thin CuO film (31 μg/cm ²) on a thick Al substrate	_	_

production cross section and bremsstrahlung cross section should be independent of these parameters. The areas of the characteristic x-ray peaks and of the selected bremsstrahlung region were estimated by the direct sum of the counts, but it was not stated which characteristic peaks were chosen to evaluate σ_K . It should be highlighted that the bremsstrahlung radiation has a marked anisotropic emission that will be blurred by the electron beam opening in the target used. The resulting anisotropy has to be included correctly in the adopted theoretical cross sections so that the K-shell ionization cross section estimates are not affected [75].

In the experiment by Llovet et al. [16] the x rays were detected by a wavelength-dispersive spectrometer (WDS) whose good energy resolution entails a better separation of the peaks. Owing to the difficulty in determining the efficiency of the WDS, a Si(Li) detector was employed to obtain a multiplicative factor based on the x-ray intensities measured with the two instruments. This procedure let them determine the absolute ionization cross section. The WDS permits a better separation of some lines than the Si(Li) spectrometer. However, there is no explanation of the lines included in the analysis or even which of them were resolved by the detectors employed. No spectrum recorded with the WDS was presented in Ref. [16], which would have helped to identify whether the equipment was able to resolve such lines. With the aim of assessing the peak adjustment procedure, the authors evaluated the $\Gamma_{K\beta}/\Gamma_{K\alpha}$ ratios and found accord within 2% with Khan and Karimi's value $\Gamma_{K\beta}/\Gamma_{K\alpha} = 0.137$ [62] that they used to determine σ_K .

Comparing our Cu K ionization cross sections with those of Llovet et~al.~[16], who employed values similar to ours for ω_K and $\Gamma_{K\beta}/\Gamma_{K\alpha}$, excellent agreement can be noted in Fig. 12. This leads us to conclude that Llovet et~al. probably included diagram and satellite lines during the peak area estimation procedure; otherwise differences $\sim 20\%$ would have arisen. With respect to the RAE counts, since it is estimated to correspond to approximately 1% of $K\alpha$ counts, and the cross section uncertainties are greater than that, it is impossible to make any statement.

V. CONCLUSIONS

Cu $K\alpha$ and $K\beta$ x-ray production cross sections have been measured using two SDDs placed at $31.1(5)^{\circ}$ and $125.0(5)^{\circ}$ with respect to the incident electron beam. The number of counts in the $K\alpha$ and $K\beta$ groups have been determined from the fit of a model function that included not only the diagram lines, but also the satellite lines of multiple vacancies and the RAE. The data at the two angles are consistent and present uncertainties of the order of 5.5%. From the $K\alpha$ x-ray production cross section, the Cu K ionization cross section has been deduced with relative uncertainties around 7.5%.

The careful analysis of the spectra also allowed us to measure the intensity ratios $\Gamma_{K\beta}/\Gamma_{K\alpha}$, $\Gamma_{RAS(KLL+KLM)}/\Gamma_{K\alpha}$, and $\Gamma_{RAS(KMM)}/\Gamma_{K\beta}$ in excellent agreement with the ratios found by other authors.

None of the cited papers that reported experimental Cu *K* ionization cross section gave details on the peak adjustment

procedure or explained which lines were taken into account in the derivation of the K-shell ionization cross section, and did not provide the values of the $\sigma_{K\alpha}^{x}$ and $\sigma_{K\beta}^{x}$. However, for these cross sections to be correctly implemented in Monte Carlo simulation codes, and also to be used in other practical applications, it is essential that it is clearly described how they were estimated and which lines and phenomena are being considered. Otherwise, the errors generated by this lack of information can amount to $\approx 20\%$ for Cu, and even more for elements with lower atomic numbers.

Although the measurement of K-shell ionization cross sections is well established since decades ago, the results of this investigation indicate that the understanding of the underlying interaction mechanisms is not yet complete. The data available, almost in its entirety, are unclear regarding the lines that are employed to deduce the x-ray production and ionization cross sections. This ambiguity jeopardises the comparison between them and, consequently, the correct interpretation of the observed discrepancies. The present discussion sheds light on this issue. As opposed to the conclusion of our previous articles concerning elements with intermediate and high atomic numbers, the discrepancy between the measured Cu K ionization cross section and the DWBA is not caused by how relativistic effects are treated in the formalism, but rather by the incorrect interpretation of which physical phenomena are considered in the peak area estimates. Since the DWBA and RDW formalisms describe single vacancy generated in the ionization event, the experimental data to be compared with these formalisms should exclude counts that come from multiple vacancies. On the other hand, often the practical interest is in the total production of x rays generated during the K-shell ionization, including single and multiple vacancy situations. We addressed both situations and found that the experimental Cu K ionization cross section agrees with the predictions of the DWBA and the RDW approximation when only the counts from single vacancies are accounted for.

Separating the lines that come from single and multiple vacancies, and the RAE counts, is a challenging task because high-resolution detectors are necessary. The results published in recent years on this topic were fundamental to resolve the Cu *K* lines with the detection system employed here. In this sense, our findings also stress the need for undertaking new experimental and theoretical studies on atomic relaxation parameters, with a clear distinction of which processes are being included in the measurements and calculations.

ACKNOWLEDGMENTS

We thank W. G. P. Engel for preparing the samples, and the technical staff of LAMFI and the São Paulo Microtron for their valuable help in the operation of the accelerator. This research was funded by the Brazilian agencies FAPESP (Fundação de Amparo à Pesquisa do Estado de São Paulo), Projects No. 13/24803-5 and No. 20/10186-8, and CNPq (Conselho Nacional de Desenvolvimento Científico e Tecnológico). The work of J.M.F.-V. is supported by the Spanish MICIU/AEI/10.13039/501100011033 through Grant No. PID2023-147112NB-C22.

DATA AVAILABILITY

The data that support the findings of this article are not publicly available upon publication because it is not technically feasible and/or the cost of preparing, depositing, and hosting the data would be prohibitive within the terms of this research project. The data are available from the authors upon reasonable request.

- X. Llovet, C. J. Powell, F. Salvat, and A. Jablonski, J. Phys. Chem. Ref. Data 43, 013102 (2014).
- [2] C. J. Powell, Rev. Mod. Phys. 48, 33 (1976).
- [3] Edited by T. D. Märk and G. H. Dunn, *Electron Impact Ionization* (Springer, New York, 1985), p. 198.
- [4] J. Trincavelli, S. Limandri, and R. Bonetto, Spectrochim. Acta Part B 101, 76 (2014).
- [5] Z. Li and U. Becker, J. Electron Spectrosc. Relat. Phenom. 237, 146893 (2019).
- [6] A. Shornikov and F. Wenander, J. Instrum. 11, T04001 (2016).
- [7] F. Salvat, PENELOPE-2018: A Code System for Monte Carlo Simulation of Electron and Photon Transport (OECD/NEA, Issy-les-Moulineaux, 2019).
- [8] B. Fischer and K. W. Hoffmann, Z. Phys. **204**, 122 (1967).
- [9] L. M. Middleman, L. R. Ford, and R. Hofstadter, Phys. Rev. A 2, 1429 (1970).
- [10] D. V. Davis, V. D. Mistry, and C. A. Quarles, Phys. Lett. A 38, 169 (1972).
- [11] K. Shima, Phys. Lett. A 77, 237 (1980).
- [12] K. Shima, T. Nakagawa, K. Umetani, and T. Mikumo, Phys. Rev. A 24, 72 (1981).
- [13] G. L. Westbrook and C. A. Quarles, Nucl. Instrum. Methods Phys. Res. Sec. B 24–25, 196 (1987).
- [14] Z. An, T. H. Li, L. M. Wang, X. Y. Xia, and Z. M. Luo, Phys. Rev. A 54, 3067 (1996).
- [15] F. Q. He, X. F. Peng, X. G. Long, Z. M. Luo, and Z. An, Nucl. Instrum. Methods Phys. Res., Sec. B 129, 445 (1997).
- [16] X. Llovet, C. Merlet, and F. Salvat, J. Phys. B: At. Mol. Opt. Phys. 33, 3761 (2000).
- [17] C. Zhou, Z. Luo, C. Tang, and Z. An, Chin. Phys. Lett. 18, 759 (2001)
- [18] R. M. Nazhmdinov, A. V. Shchagin, S. V. Trofymenko, I. A. Kishin, A. S. Kubankin, A. P. Potylitsyn, A. S. Gogolev, N. A. Filatov, G. Kube, N. A. Potylitsina-Kube, M. Stanitzki, and A. Novokshonov, J. Phys. B: At. Mol. Opt. Phys. 54, 045201 (2021).
- [19] L. G. Parrat, Phys. Rev. 50, 1 (1936).
- [20] T. L. Pham, T. V. B. Nguyen, J. A. Lowe, I. P. Grant, and C. T. Chantler, J. Phys. B: At. Mol. Opt. Phys. 49, 035601 (2016).
- [21] T. Åberg, Phys. Rev. A 4, 1735 (1971).
- [22] M. M. Bé, M. C. Lépy, J. Plagnard, and B. Duchemin, Appl. Radiat. Isot. 49, 1367 (1998).
- [23] M. Deutsch, E. Förster, G. Hölzer, J. Härtwig, K. Hämäläinen, C. C. Kao, S. Huotari, and R. Diamant, J. Res. Natl. Inst. Stand. Technol. 109, 75 (2004).
- [24] S. P. Limandri, R. D. Bonetto, A. C. Carreras, and J. C. Trincavelli, Phys. Rev. A 82, 032505 (2010).
- [25] S. P. Limandri, A. C. Carreras, R. D. Bonetto, and J. C. Trincavelli, Phys. Rev. A 81, 012504 (2010).
- [26] Y. Ito, T. Tochio, H. Ohashi, M. Yamashita, S. Fukushima, M. Polasik, K. Slabkowska, L. Syrocki, E. Szymánska, J. Rzadkiewicz, P. Indelicato, J. P. Marques, M. C. Martins,

- J. P. Santos, and F. Parente, Phys. Rev. A **94**, 042506 (2016).
- [27] Y. Ito, T. Tochio, M. Yamashita, S. Fukushima, A. M. Vlaicu, L. Syrocki, K. Slabkowska, E. Weder, M. Polasik, K. Sawicka, P. Indelicato, J. P. Marques, J. M. Sampaio, M. Guerra, J. P. Santos, and F. Parente, Phys. Rev. A 97, 052505 (2018).
- [28] H. A. Melia, C. T. Chantler, L. F. Smale, and A. Illig, Acta Cryst. A75, 527 (2019).
- [29] H. A. Melia, C. T. Chantler, L. F. Smale, and A. Illig, J. Phys. B: At. Mol. Opt. Phys. 53, 195002 (2020).
- [30] O. C. B. Santos, V. R. Vanin, N. L. Maidana, M. N. Martins, M. H. Tabacniks, C. L. Rodrigues, T. F. Silva, A. D. Santos, S. F. Barros, J. A. García-Alvarez, M. F. Koskinas, J. M. Fernández-Varea, and M. S. Pindzola, Phys. Rev. A 100, 022703 (2019).
- [31] S. F. Barros, V. R. Vanin, N. L. Maidana, A. A. Malafronte, J. M. Fernández-Varea, and M. S. Pindzola, Phys. Rev. A 105, 012818 (2022).
- [32] V. R. Vanin, N. L. Maidana, A. Mangiarotti, R. R. Lima, A. A. Malafronte, S. F. Barros, and M. N. Martins, Radiat. Phys. Chem. 154, 26 (2019).
- [33] T. F. Silva, C. L. Rodrigues, M. Mayer, M. V. Moro, G. F. Trindade, F. R. Aguirre, N. Added, M. A. Rizzutto, and M. H. Tabacniks, Nucl. Instrum. Methods Phys. Res. Sec. B 371, 86 (2016).
- [34] M. Mayer, AIP Conf. Proc. 475, 541 (1999).
- [35] M. M. Bé, N. Coursol, B. Duchemin, F. Lagoutine, J. Legrand, K. Debertin, E. Schönfeld, Table of radionuclides, http://www. lnhb.fr/home/nuclear-data/ (LNE-LNHB/CEA, Gif-sur-Yvette, 2011).
- [36] M. C. Lépy, J. Plagnard, and L. Ferreux, Appl. Radiat. Isot. 66, 715 (2008).
- [37] M. Rodrigues, M. L. Loidl, and S. Pierre, Metrologia 60, 025005 (2023).
- [38] S. M. Seltzer, Nucl. Instrum. Meth. 188, 133 (1981).
- [39] S. F. Barros, N. L. Maidana, J. M. Fernández-Varea, and V. R. Vanin, X-ray Spectrom. 46, 34 (2017).
- [40] Amptek Inc., Detector efficiency FAQ, https://www.amptek. com/internal-products/obsolete-products/sdd-x-ray-detectorsfor-xrf/x-123sdd-complete-x-ray-spectrometer-with-silicondrift-detector-sdd (2024).
- [41] S. F. Barros, V. R. Vanin, A. A. Malafronte, N. L. Maidana, and M. N. Martins, J. Synchrotron Radiat. 25, 484 (2018).
- [42] J. M. Fernández-Varea, V. Jahnke, N. L. Maidana, A. A. Malafronte, and V. R. Vanin, J. Phys. B: At. Mol. Opt. Phys. 47, 155201 (2014).
- [43] S. M. Seltzer and M. J. Berger, At. Data Nucl. Data Tables 35, 345 (1986).
- [44] L. Kissel, C. A. Quarles, and R. H. Pratt, At. Data Nucl. Data Tables 28, 381 (1983).
- [45] S. F. Barros, V. R. Vanin, N. L. Maidana, M. N. Martins, J. A. García-Alvarez, O. C. B. Santos, C. L. Rodrigues, M. F.

- Koskinas, and J. M. Fernández-Varea, J. Phys. B: At. Mol. Opt. Phys. **51**, 025201 (2018).
- [46] K. Tsutsumi, H. Nakamori, and K. Ichikawa, Phys. Rev. B 13, 929 (1976).
- [47] H. Enkisch, C. Sternemann, M. Paulus, M. Volmer, and W. Schülke, Phys. Rev. A 70, 022508 (2004).
- [48] O. Mauron, J. C. Dousse, J. Hoszowska, J. P. Marques, F. Parente, and M. Polasik, Phys. Rev. A 62, 062508 (2000).
- [49] H. Verma, J. Phys. B: At. Mol. Opt. Phys. 33, 3407 (2000).
- [50] M. Kavčič, Phys. Rev. A 68, 022713 (2003).
- [51] M. Fritsch, C. C. Kao, K. Hamalainen, O. Gang, E. Förster, and M. Deutsch, Phys. Rev. A 57, 1686 (1998).
- [52] M. Deutsch, G. Hölzer, J. Härtwig, J. Wolf, M. Fritsch, and E. Förster, Phys. Rev. A 51, 283 (1995).
- [53] F. Gao, L. W. Campbell, R. Devanathan, Y. L. Xie, Y. Zhang, A. J. Peurrung, and W. J. Weber, Nucl. Instrum. Methods Phys. Res. Sec. A 579, 292 (2007).
- [54] J. L. Campbell, A. Perujo, W. J. Teesdale, and B. M. Millman, Phys. Rev. A 33, 2410 (1986).
- [55] J. L. Campbell, Nucl. Instrum. Methods B 22, 13 (1987).
- [56] G. B. Baptista, J. Phys. B: At. Mol. Opt. Phys. 34, 389 (2001).
- [57] R. D. Deslattes, E. G. Kessler, Jr, P. Indelicato, L. de Billy, E. Lindroth, and J. Anton, Rev. Mod. Phys. **75**, 35 (2003).
- [58] J. H. Scofield, At. Data Nucl. Data Tables 14, 121 (1974).
- [59] M. O. Krause and J. H. Oliver, J. Phys. Chem. Ref. Data 8, 329 (1979).
- [60] O. Mauron and J.-C. Dousse, Phys. Rev. A 66, 042713 (2002).
- [61] G. Hölzer, M. Fritsch, M. Deutsch, J. Härtwig, and E. Förster, Phys. Rev. A **56**, 4554 (1997).
- [62] M. R. Khan and M. Karimi, X-ray Spectrom. 9, 32 (1980).
- [63] S. F. Barros, A. R. Petri, A. A. Malafronte, J. M. Fernández-Varea, N. L. Maidana, M. N. Martins, T. F. Silva, V. R.

- Vanin, and A. Mangiarotti, Radiat. Phys. Chem. 202, 110540 (2023).
- [64] S. F. Barros, V. R. Vanin, A. Mangiarotti, N. L. Maidana, and J. M. Fernández-Varea, Phys. Rev. A 100, 062705 (2019).
- [65] P. M. DeLuca, The international commission on radiation units and measurements, J. ICRU 7, 5 (2007).
- [66] H. R. Redus, A. C. Huber, and D. J. Sperry, Dead time correction in the DP5 digital pulse processor, in 2008 IEEE Nuclear Science Symposium Conference Record (IEEE, Piscataway, NJ, 2008), pp. 3416–3420.
- [67] W. Bambynek, B. Crasemann, R. W. Fink, H. U. Freund, H. Mark, C. D. Swift, R. E. Price, and P. V. Rao, Rev. Mod. Phys. 44, 716 (1972).
- [68] J. H. Hubbell, P. N. Trehan, N. Singh, B. Chand, D. Mehta, M. L. Garg, R. R. Garg, S. Singh, and S. Puri, J. Phys. Chem. Ref. Data 23, 339 (1994).
- [69] M. O. Krause, J. Phys. Chem. Ref. Data 8, 307 (1979).
- [70] T. Yashoda, S. Krishnaveni, and R. Gowda, Nucl. Instrum. Methods Phys. Res., Sect. B 240, 607 (2005).
- [71] W. Cao, M. Kavčič, J. Cl. Dousse, M. Berset, K. Bučar, M. Budnar, K. Fennane, J. Hoszowska, Y.-P. Maillard, J. Szlachetko, M. Szlachetko, and M. Žitnik, Phys. Rev. A 83, 042513 (2011).
- [72] R. K. Singh and R. Shanker, Phys. Rev. A 67, 012708 (2003).
- [73] D. Bote and F. Salvat, Phys. Rev. A 77, 042701 (2008).
- [74] P. Palmeri, P. Quinet, and D. Batani, At. Data Nucl. Data Tables 102, 1 (2015).
- [75] J. A. García-Alvarez, J. M. Fernández-Varea, V. R. Vanin, O. C. B. Santos, S. F. Barros, A. A. Malafronte, C. L. Rodrigues, M. N. Martins, M. F. Koskinas, and N. L. Maidana, J. Phys. B: At. Mol. Opt. Phys. 50, 155003 (2017).